1 Changes in global teleconnection patterns under global warming and stratospheric aerosol

2 intervention scenarios

3 **Abolfazl Rezaei[1,2], Khalil Karami[3], Simone Tilmes[4], & John C. Moore[5, 6, 7]**

5 [1] Department of Earth Sciences, Institute for Advanced Studies in Basic Sciences, Zanjan 45137–

6 66731, Iran. arezaei@iasbs.ac.ir; abolfazlrezaei64@gmail.com.

7 [2] Center for Research in Climate Change and Global Warming (CRCC), Institute for Advanced Studies

8 in Basic Sciences (IASBS), Zanjan 45137–66731, Iran.

9 [3] Institut für Meteorologie, Stephanstraße 3, 04103 Leipzig, Germany. khalil.karami@uni-leipzig.de

10 [4] National Center for Atmospheric Research, Boulder, CO, USA. tilmes@ucar.edu

11 [5] College of Global Change and Earth System Science, Beijing Normal University, Beijing, 100875,

12 China. john.moore.bnu@gmail.com

13 [6] CAS Center for Excellence in Tibetan Plateau Earth Sciences, Beijing, 100101, China.

14 [7] Arctic Centre, University of Lapland, Rovaniemi, 96101, Finland.

16 **Abstract**

17 We investigate the potential impact of Stratospheric Aerosol Intervention (SAI) on the

18 spatiotemporal behavior of large-scale climate teleconnection patterns represented by the North

19 Atlantic Oscillation (NAO), Pacific Decadal Oscillation (PDO), El Niño/Southern Oscillation (ENSO)

20 and Atlantic Multidecadal Oscillation (AMO) indices using simulations from the Community Earth

21 System Models (CESM1 and CESM2). The leading Empirical Orthogonal Function of sea surface

22 temperature (SST) anomalies indicates that greenhouse gas forcing is accompanied by increases in

23 variance across both the North Atlantic (i.e., AMO) and North Pacific (i.e., PDO) and a decrease over

24 the tropical Pacific (i.e., ENSO); however, SAI effectively reverses these global warming-imposed

25 changes. The projected spatial patterns of SST anomaly related to ENSO show no significant change

26 under either global warming or SAI. In contrast, the spatial anomaly patterns pertaining to AMO (i.e.,

27 in the North Atlantic) and PDO (i.e., in the North Pacific) changes under global warming are effectively

28 suppressed by SAI. For AMO, the low contrast between the cold-tongue pattern and its surroundings

29 in the North Atlantic, predicted under global warming, is restored under SAI scenarios to similar

30 patterns as in the historical period. The frequencies of El Niño and La Niña episodes increase with

31 greenhouse gas emissions in the models, while SAI tends to compensate for them. All climate indices'

32 dominant modes of inter-annual variability are projected to be preserved in both warming and SAI

33   scenarios. However, the dominant decadal and interdecadal variability mode changes induced by

34   global warming are exacerbated by SAI, particularly in the Atlantic-based AMO.

35   **Keywords:** Ocean-atmosphere teleconnections; GLENS; SSP5-85; Stratospheric Aerosol

36   Intervention; Global warming

37

38   **500-character non-technical text**

39   Teleconnections are important characteristics of the climate system, well-known examples include

40   the El Niño and La Niña events driven from the tropical Pacific. We examined how patterns that arise

41   in the Pacific and Atlantic Oceans behave under stratospheric aerosol geoengineering and

42   greenhouse gas-induced warming. In general, geoengineering reverses trends, however in the

43   Atlantic, the multidecadal oscillations that are shifted to higher frequencies by greenhouse gas are

44   further strengthened.

45

46   **1. Introduction**

47   Although the Paris agreement and accompanying international commitments to decrease carbon

48   emissions are an essential step forward, current nationally contributions have only about a 50%

49   chance to restrict global mean temperature increase to 2°C above preindustrial (Meinshausen et al.,

50   2022). Exceeding 2°C will lead to severe consequences and societal disruption worldwide as

51   humanity is critically dependent on ecosystems, food, fresh water, and health systems which face

52   rapidly challenging adaptation pressure above 2°C of global warming (Field and Barros, 2014).

53   In parallel with emissions reductions, solar radiation modification (SRM) has been suggested to limit

54   global temperature increases and consequent climate impacts from anthropogenic greenhouse gas

55   emissions. A naturally occurring analog of SRM is the well-known global surface cooling following

56   large volcanic eruptions, albeit over relatively short periods. Simulations have shown that SRM

57   decreasing total solar irradiance by about 2%, would roughly compensate for global warming from a

58   doubling of CO_2 concentrations (Dagon and Schrag, 2016).

59   Oceans act as major drivers of climate variability worldwide (e.g., Shukla, 1998; Cai et al., 2021), and

60   more than 90% of the excess energy balance of the earth arising from greenhouse gas emissions ends

61   up heating the ocean (Cheng et al., 2015). Variations in sea surface temperatures (SSTs) and the

62   global climate are linked through ocean-atmosphere energy exchanges that can be helpfully

63   summarized by climate indices that characterize large-scale teleconnection patterns. That is

64   recurring and persistent, large-scale anomaly patterns of pressure and circulation across large

65   geographical regions. Some of the most referred to are El Niño/Southern Oscillation (ENSO), Pacific

66   Decadal Oscillation (PDO), Atlantic Multidecadal Oscillation (AMO), and North Atlantic Oscillation

67   (NAO). The dominant inter-annual feature of climate variability on the planet is ENSO, and its state

68   produces widespread climatic and environmental outcomes (Latif and Keenlyside, 2009). The PDO

69   modulates marine ecosystems and global climate on decadal time scales (Mantua et al., 1997),

70   impacts ENSO onset and frequency (Fang et al., 2014), and is useful for short- to long-term climate

71   forecast (An and Wang, 1999). The AMO has broader hemispheric impacts beyond North American

72   and European climates (Enfield et al. 2001), influencing the monsoons across North African, East

73   Asia, and India (Zhang and Delworth 2006). The NAO is among the dominant climate variability

74   modes in the northern hemisphere (Simpkins, 2021).

75   Several studies have explored how climate indices, particularly ENSO, respond to global warming

76   and increasing greenhouse gas concentrations. Statistically significant systemic changes have

77   occurred in ENSO dynamics and the evolution of El Niño and La Niña events since the 1960s (Moron

78   et al., 1998; Capotondi and Sardeshmukh, 2017). ENSO may favor more severe events under global

79   warming (Fedorov and Philander, 2001), and Cai et al. (2015) found that ENSO-associated disastrous

80   weather consequences tend to arise more frequently under unabated CO_2 emissions. Cai et al. (2021)

81   found an inter-model consensus on increases in forthcoming ENSO rainfall and temperature

82   fluctuations under increasing greenhouse gas concentrations. The PDO, which is essentially the

83   extra-tropical manifestation of ENSO, is simulated with a similar spatial pattern as at present under

84   various future climates but with reduced amplitude and a shorter characteristic time scale (e.g.,

85   Zhang and Delworth, 2016). The North Atlantic is a key ocean for investigating global climate

86   changes (Wang and Dong, 2010), and acts as a major carbon dioxide sink (Watson et al., 2009).

87   Atmospheric CO_2 concentrations vary with the phase of the AMO with the warm phase associated

88   with lowered atmospheric CO2 (Wang and Dong, 2010). The response of NAO to greenhouse gas

89   warming is not yet conclusive, but sea surface temperature both in the North Atlantic and the

90   conditions in the Arctic via the linkages between the NAO and the Arctic Oscillation and hence the

91   stratosphere are important (Hamouda et al., 2021).

92   Stratospheric Aerosol Intervention (SAI), is a type of SRM that has been widely simulated by many

93   global climate models (e.g., Kravitz et al., 2013), which is accompanied by changing in global

94   circulations such as the NAO teleconnection pattern (Moore et al., 2014), and is known in various

95   models to partially offset the decline in the Atlantic Meridional Overturning Circulation (AMOC; Xie

96   et al., 2022). Undorf et al. (2018) simulated the North Atlantic SST cooling accompanied by the

97   historical rise of stratospheric sulfate aerosol from North America and Europe dating back to 1850-

98   1975. Gabriel and Robock (2015) is the only study to date that explores the effects of SAI in multiple

99   models on the possible amplitude and frequency changes of El Niño/Southern Oscillation (ENSO).

100   They concluded that changes in ENSO in the SAI simulations were either not present or not large

101   enough to be captured by their approach, given the across-model variability issue. Thus, little is

102   known about possible changes that future global climate change scenarios with artificial cooling may

103   have on ocean-atmosphere climate indices. Recently, a novel set of SRM models have been globally

104   complete with the state-of-the-art climate models: Community Earth System Model versions 1 and

105   2 (CESM1 and CESM2). These models have improved planetary boundary layer turbulence, aerosols,

106   radiation, and cloud microphysics which should enable more reliable for the forthcoming global

107   climate change projections (Mills et al., 2017).

108   We use the Geoengineering Large Ensemble Simulation (GLENS) with 20 members from a single

109   model, the Community Earth System Model 1 (CESM1) with Stratospheric Aerosol Intervention

110   (GLENS-SAI), to explore the possible changes in teleconnection under future climate change

111   scenarios. The models use the Representative Concentration Pathway (RCP) 8.5 high greenhouse gas

112   emissions forcing state (Riahi et al., 2011) as a baseline and increase stratospheric sulfur injections

113   through the century, to maintain global surface temperatures at 2020 levels. This produces an

114   increasingly large signal-to-noise ratio through the 21st century. In addition, we use recent

115   simulations (SSP5-8.5-SAI) with an updated model version (CESM2). For these simulations, the SSP5-

116   8.5 greenhouse gas emissions scenarios were used as the greenhouse gas baseline scenario on which

117   SAI was performed. The two different model experiments show some surprising differences in the

118   required sulfur injections and climate outcomes with and without SAI applications (Tilmes et al.,

119   2020, Fasullo et al., 2020). Thus, even models from different generations in the same family can

120   produce sufficiently different climates to explore a range of plausibly real climate impacts. The goal

121   of this study is to identify robust features across the two model versions in the response of climate

122   indices (ENSO, PDO, AMO and NAO) to greenhouse gas induced global warming and its compensation

123   by SAI.

124   We employed empirical orthogonal functions and wavelet transforms to decompose time series and

125   study the differences in the teleconnection indices between the SSP5-8.5 and SSP5-8.5-SAI scenarios.

126   Since teleconnection patterns are emergent features of the non-linear, chaotic climate system (Ghil

127   et al., 2002), their underlying physical causes are complex and not necessarily the same in any model

128   as on the real planet. Hence, we assess the potential changes in temporal and spatial characteristics

129   of climate indices of AMO, NAO, ENSO, and PDO under both extreme warming greenhouse scenarios

130   and with SAI employed to mitigate those warmings while maintaining extreme greenhouse gas

131   concentration trajectories.

2. Data and Methods

2.1. Models and scenarios

We used two SAI models and scenarios: (1) CESM1 for GLENS-SAI and (2) CESM2 for SSP5-8.5-SAI.
The GLENS (Geoengineering Large Ensemble) project used the RCP8.5 as a baseline scenario (Tilmes
et al., 2018). Simulations were done by the Community Earth System Model version 1 (CESM1) with
the Whole Atmosphere Community Climate Model (WACCM) as the atmospheric system integrated
to land, ocean, and sea ice models (Mills et al., 2017). The resolution of atmospheric component is
1.25° in longitude and 0.9° in latitude. A 20-member reference simulation for the RCP8.5 scenario
(Riahi et al., 2011) over the 2010–2030 period with three ensemble members (001 to 003)
continuing up to the end of the 21st century. GLENS-SAI is a 20-member ensemble of stratospheric
sulfur dioxide (SO_2) injection simulations, spanning 2020-2099. This experiment was designed to
keep the mean surface temperature at 2020 global conditions, and also stabilize interhemispheric
and equator-to-pole surface temperature gradients at 2020 values while forced by the RCP8.5
greenhouse gas scenario. Stratospheric injections were performed at four different latitudes (15°N
and 15°S at 25 km, 30°N and 30°S), at 22.8 km, and at 180° longitude using a feedback control
algorithm (Kravitz et al., 2017; Tilmes et al., 2018). Each ensemble member was begun in 2010 with
small differences in their initial air temperatures, while their ocean, sea-ice, and land temperatures
were the same. Even before the start of the SAI injections in 2020, the fully coupled model produced
variability between the ensemble members due to its chaotic nature. Here, we use all available
members of the RCP8.5 and GLENS-SAI simulations, which extend until the end of the 21st century.
For the analysis, we used monthly SST and sea-level pressure (PSL).

We also analyzed output from the NCAR Community Earth System Model version 2- Whole
Atmosphere Community Climate Model Version 6 (CESM2(WACCM6)). This model version was used
for performing the Coupled Model Intercomparison Project Phase 6 (CMIP6; Eyring et al., 2016)
simulations. Like GLENS, this SAI experiment is according to the high greenhouse gas emissions
scenario, called SSP5-85 in CMIP6, (SSP5-8.5-SAI) and limits mean global temperatures to 1.5°C
above 1850–1900 conditions, which without SAI, is exceeded around the year 2020 in
CESM2(WACCM6) under SSP5-8.5. The experiment used sulfur injection locations at the same four
latitudes as in GLENS to accomplish the same three temperature goals (Tilmes et al., 2020). We used
the monthly SST and PSL data from all five members (r1 to r5) of the SSP5-8.5 scenario (covering
2015-2100) and the three available ensemble members of SSP5-8.5-SAI that cover the period of
2020-2100. For the analysis, we also applied a one-member historical simulation based on the
specific CESM1(WACCM) version used for GLENS between 1980-2009 (denoted as "historical" in the

165 following). All three corresponding members (r1 to r3) from the CESM2(WACCM6) version were

166 used for the historical period.

167

168 **2.2. Climate indices**

169 The AMO was calculated from the area-weighted average of SSTs across the northern Atlantic from

170 0-70° N. The NAO was computed from the PSL time series at two stations: Gibraltar (to the south of

171 Spain; around 36.1°N and 5.3°W) and Reykjavik (in the southwest of Iceland; around 64.1°N and

172 22.0°W). The ENSO index follows the definition proposed by Trenberth (1997). Here, we used SSTs

173 at the Niño 3.4 region (east-central equatorial Pacific between 5°N-5°S, 170°W-120°W) as a proxy

174 for ENSO. After removing the global mean SST anomaly, the leading Empirical Orthogonal Function

175 (EOF) of monthly SST anomalies across the North Pacific (20°–70°N) is termed PDO following Mantua

176 et al. (1997). All these computations were analyzed through the Climate Data Toolbox prepared by

177 Greene et al. (2019).

178 We characterized ENSO by El Niño and La Niña episodes. The ENSO index positive and negative

179 episodes correspond to El Niño and La Niña respectively. Consistent with Gabriel and Robock (2015),

180 ENSO episodes were identified as departures of at least 0.5 standard deviations from zero in a five-

181 month running averaged ENSO time series. Each episode was characterized by its duration (years),

182 the extreme peak excursion (°C), and the width at half extreme height (years).

183

184 **2.3. Spatio-temporal analyses**

185 Analyses in both space and time as well as modes of variability ranging from the inter-annual through

186 decadal, to inter-decadal changes were used to identify the possible changes in the large-scale climate

187 circulations resulting from global warming and SAI scenarios. EOF analysis is commonly used to

188 extract the climate variability space-time modes (e.g., Chen and Tung, 2018; Joyce, 2002). We applied

189 EOF to extract the first (dominant) modes of de-trended non-seasonal-SST and its corresponding

190 variance across the North Atlantic and North Pacific, which are related to the AMO and PDO

191 respectively. As ENSO is the primary indicator of global climate variability, we used the leading EOF

192 of global SST anomalies in the study of ENSO.

193 The continuous wavelet transform (CWT) is commonly used to capture the primary characteristics

194 of signals (Addison, 2018). For a time series (x_n, n=1, . . . , N) having regular time intervals δt, the

195 CWT is computed as the convolution of x_n with the scaled and normalized wavelet (e.g., here we use

196 the Morlet wavelet which gives reasonably equal weighting and resolution in time and period space;

197 Grinsted et al., 2004):

198 $$W_n^X(s) = \sqrt{\frac{\delta t}{s}} \sum_{n'=1}^{N} x_{n'} \psi_0 \left[(n'-n)\frac{\delta t}{s} \right], \quad \psi_0(\eta) = \pi^{-1/4} e^{i\omega_0 \eta} e^{-0.5\eta^2}$$ (1)

199 where s is the wavelet scale, ψ_0 the Morlet wavelet, ω_0 dimensionless frequency, [*] the complex

200 conjugate, and η dimensionless time. The noise spectrum assigned to generate significance testing

201 is a key issue in time series analysis. We concurred with the widely-used red-noise null hypothesis

202 methodology based on 1000 synthetic series with the same mean, standard deviation and first-order

203 autoregressive coefficient as the target time series produced by Monte Carlo approaches to estimate

204 the significance of the CWT (Grinsted et al., 2004). Additionally, for each time series, CWT's global

205 power spectrum was calculated as a function of time. The global power spectrum provides insight

206 into the dominant temporal modes of variability of each climate index within each ensemble member

207 for the reference greenhouse gas and SAI scenarios.

208 The individual ensemble members are treated as independent of each other in calculating the

209 statistics of the ensembles. The CWT was conducted on monthly ENSO time series, and the 12-month

210 moving averaged low-pass filtered signals of AMO, NAO, and PDO. We always use the longest

211 available record length in every ensemble member to gain maximum statistical power to establish

212 significant differences between experiments.

213

214 **3. Results:**

215 **3.1. Changes in the spatial patterns**

216 Figure 1 reveals the projected changes in the variance of the SST anomalies related to the AMO (i.e.,

217 across the North Atlantic), ENSO (i.e., global scale), and PDO (i.e., across the North Pacific) based on

218 CESM1 and CESM2 results. There are three different plots for the CESM1 as the time period of the 20-

219 member ensemble for RCP8.5 differ: ensembles 001 to 003 (2010-2097) are longer than the other

220 17 ensemble members (2010-2030). For RCP8.5 and SSP5-85 using CESM1 and CESM2, respectively,

221 the strong greenhouse gas forcing and global warming to the end of the 21st century increases the

222 variance of the first EOF SST anomaly in the North Atlantic and North Pacific (representing AMO and

223 PDO), but reduces the variance of the leading EOF in global SST anomaly (related to ENSO). SAI in

224 CESM2 effectively restores the projected changes in the leading EOF variance of each index due to

225 greenhouse gas forcing to its historical values. The lack of statistics for the CESM1 historical scenarios

226 prevents firm conclusions for that model.
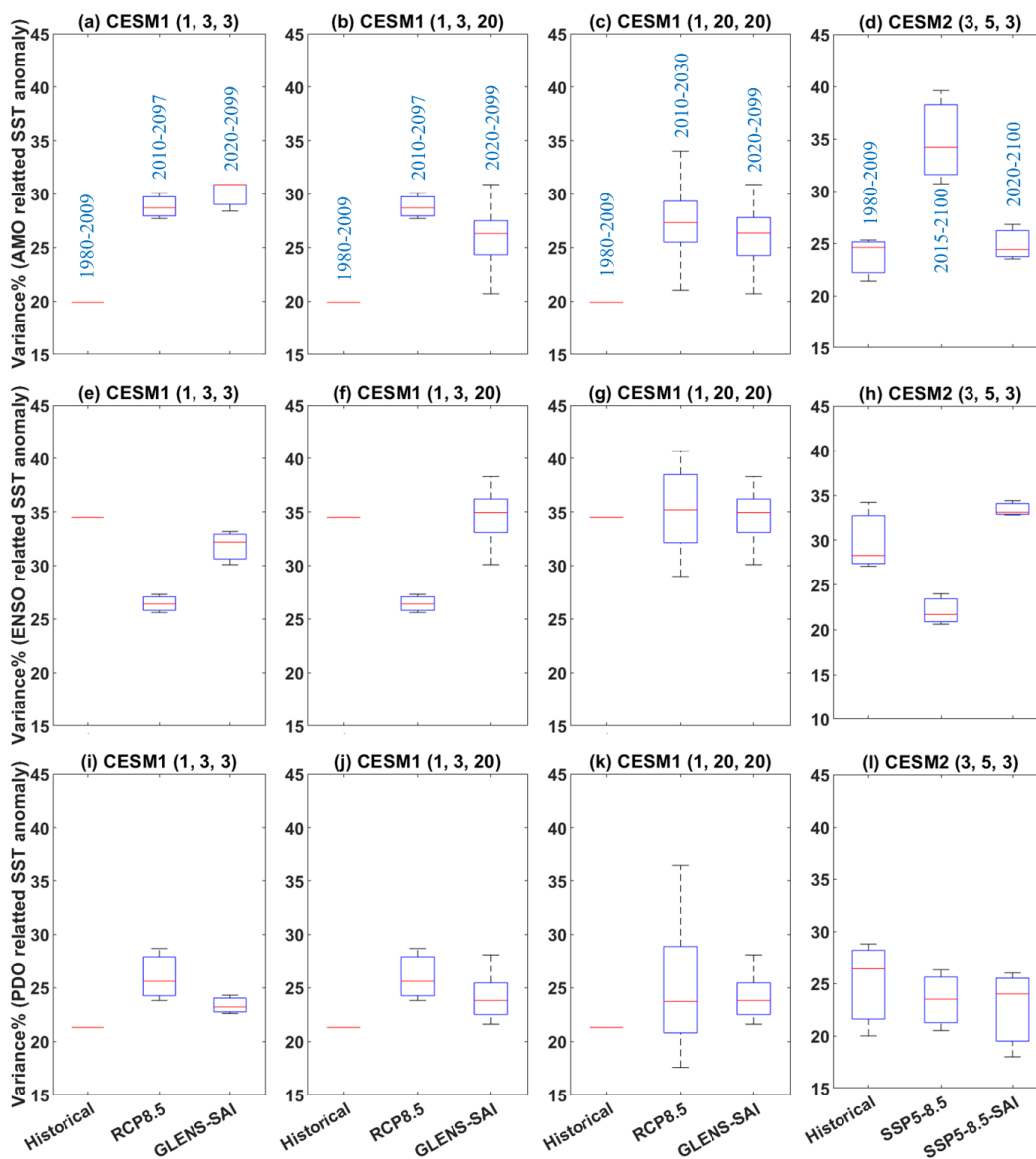
Figure 1. Box and whiskers plot of the variance in the leading EOFs, representing AMO, PDO, and ENSO, relative to the total variance of the SST fields: AMO across the North Atlantic (top row); ENSO (middle row) global SST; and PDO across the North Pacific (bottom row). The values in blue on each column box in the upper row show the period of the data for historical, greenhouse gas (i.e., RCP-8.5 and SSP5-8.5), and climate intervention (GLENS-SAI and SSP5-8.5-SAI) scenarios. The titles of each subplot refer to the CESM version and the number of ensembles used in the historical, greenhouse gas (RCP8.5 and SSP5-8.5), and SAI (GLENS-SAI or SSP5-8.5-SAI) scenarios, respectively. The median for each experiment is denoted by the red line, the upper (75th) and lower (25th) quartiles by the top and bottom of the box and ensemble limits by the whisker extents.

237   Figures 2-5 and S1-S2 (in Supporting Information) show the spatial anomalies of the leading EOF

238   mode of the SST in the North Atlantic and North Pacific under both the CESM1 and CESM2. For the

239   historical period, there is a cold-tongue pattern in the North Pacific broaden from the western to the

240   eastern parts surrounded by warm water, particularly to the north. Greenhouse gas related global

241   warming lowers the contrast between the cold-tongue pattern and its surroundings and increases

242   the water temperature inside the cold-tongue-pattern, and also leads to a substantial expansion of a

243   warm-pattern in the north. The same patterns (shown in Fig. 3) are also obtained under SSP5-8.5

244   using CESM2. SAI effectively shrinks the warm pattern in the northern Atlantic under the RCP8.5 and

245   SSP5-8.5. The SSP5-8.5-SAI experiment increases the temperature contrast in the cold-tongue

246   pattern, while the GLESN-SAI does not. The projected changes in the spatial SST patterns across the

247   North Atlantic, observed under global warming, are largely suppressed under SAI. This response of

248   AMO to SAI is compatible with the observed changes in AMO imposed by anthropogenic and volcanic

249   aerosols reported by Masson-Delmotte et al. (2021). Anthropogenic and volcanic aerosols are

250   understood to have impacted the timing and magnitude of the cold (negative) episode in the

251   historical AMO record between the mid-1960s and mid-1990s and succeeding warming (Masson-

252   Delmotte et al., 2021). Anthropogenic aerosols have also been suspected as impacting historical SSTs

253   elsewhere, particularly the decadal ENSO variability (e.g., Sutton and Hodson, 2007; Westervelt et al.,

254   2018).

255
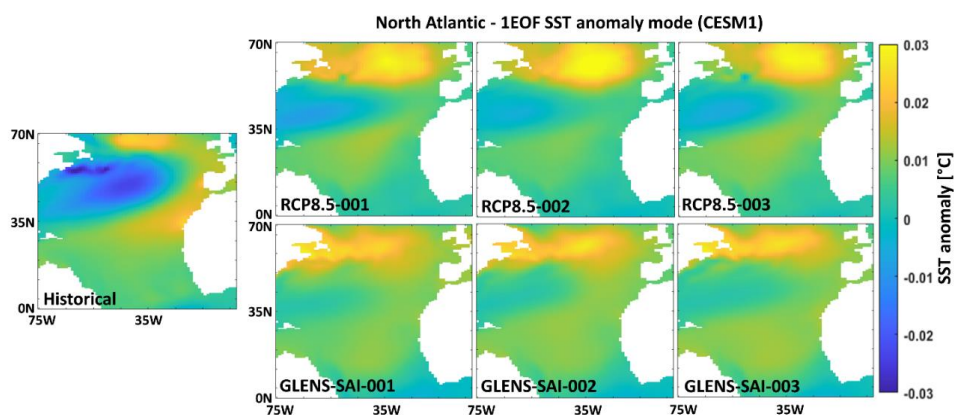
256

257   **Figure 2.** The first EOF (1EOF) patterns of SST anomaly across the North Atlantic relate to the AMO
258   index simulated by CESM1 for the historical data and the three ensemble members (001 to 003)
259   outputs under the RCP8.5 and GLENS-SAI scenarios.
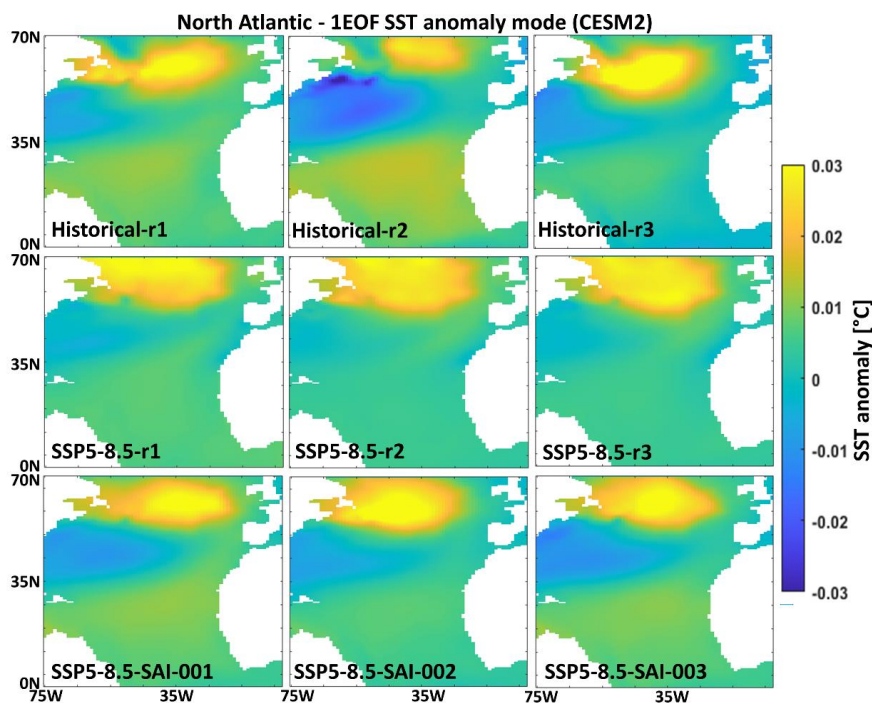
Figure 3. As in Fig. 2, but for CESM2 and SSP5-8.5. r1 to r3 denote to the variant labels (i.e., ensemble members).

The leading EOF of monthly global SST anomalies corresponding to the ENSO mode (Figs. S1 and S2), and is seen as a warm-tongue pattern over the tropical Pacific, that exhibits very similar patterns under both global warming and SAI scenarios as in the historical period. However, Fig. S3 shows that the warm-tongue pattern in CESM1 and CESM2 has an excessive westward extension relative to observations, which is compatible with the findings of Capotondi et al. (2020).

While the first EOF SST anomaly across the North Pacific under both global warming and SAI scenarios in CESM1 and CESM2 (Figs. 4 and 5) exhibits a similar cold-tongue pattern (typical of the North Pacific) as in the historical period, a lower contrast between the cold-tongue pattern and its surroundings is observed under SSP5-8.5 (Fig. 5), which is effectively compensated by the geoengineering scenarios of SSP5-8.5-SAI. There is an excessive eastward expansion of the cold-tongue pattern with cooler temperatures under the SAI scenario as simulated by the CESM1 (Fig. 4), which is due to the cooling of the water imposed by the SO_2 injection.
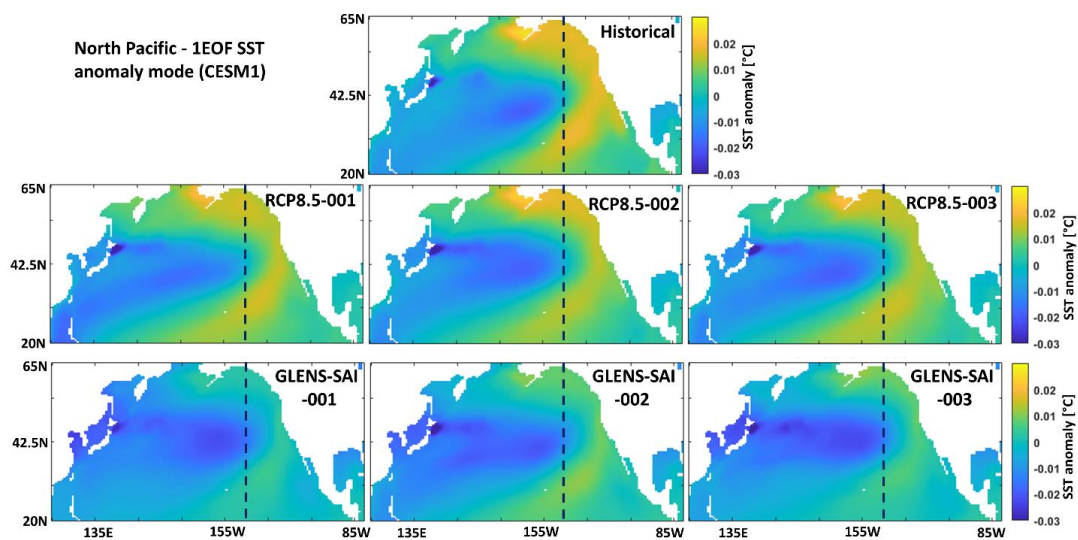
Figure 4. The first EOF (1EOF) modes of SST anomaly across the North Pacific relate to the PDO index in CESM1 for the historical data and the three ensemble members (001 to 003) output from the RCP8.5 and GLENS-SAI scenarios.
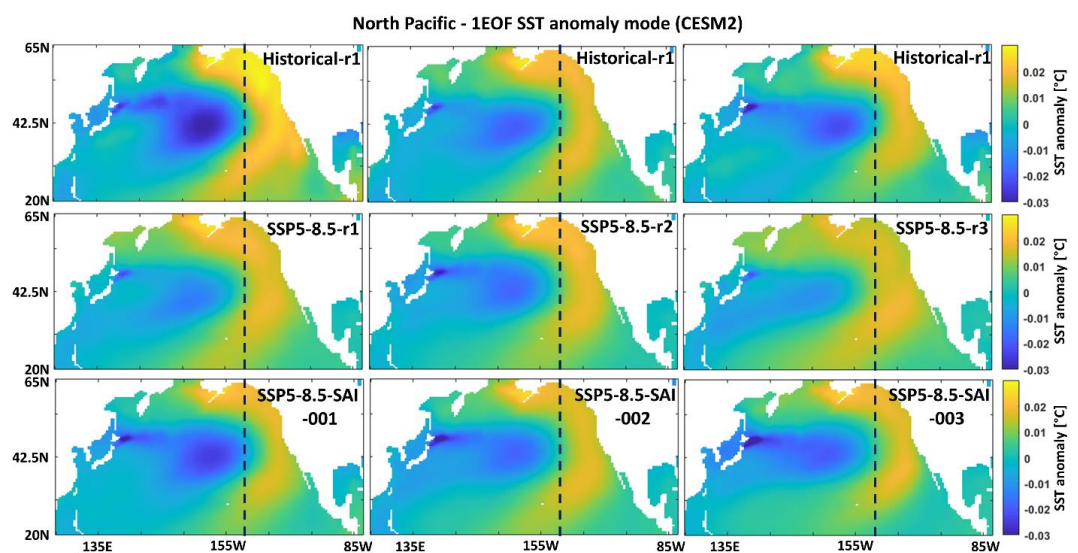
Figure 5. As in Fig. 4, but for CESM2.

3.2. Temporal evolution of indices

Figure 6 displays the projected changes in the El Niño and La Niña episodes in the ENSO index under global warming and SAI. Although the global warming scenario simulated by CEMS2 tends to reduce the time between, as well as the intensity and duration of the El Niño and La Niña episodes compared to the historical conditions, this is less clear for CESM1. CESM2 results suggest that with greenhouse gases risings, the frequency of the El Niño and La Niña episodes increases (right panel of Fig. 6), which is supported by earlier research on climate simulations e.g., Fredriksen et al., (2020); Cai et al. (2014) and Yun et al. (2021) for El Niño, and Cai et al. (2015) for La Niña. The mean peak interval in CESM2 presented in Fig. 6j (6g) decreases from 3.72 (3.28) in the historical period to 3.11 (3.20) years for the La Niña (El Niño) events in the SSP5-85 scenario. Nonetheless, for both SAI experiments using CESM1 and CESM2, the peak intervals, height (i.e., intensity), and width (i.e., duration) of both the El Niño and La Niña episodes are found to increase relative to the global warming scenarios without SAI, except for La Niña under CECM1 which shows a small decrease (Fig. 6f). However, while CESM2 provides more ensemble members over the historical period, SAI tends to compensate for the changes in frequency, intensity, and duration of the El Niño and La Niña episodes.
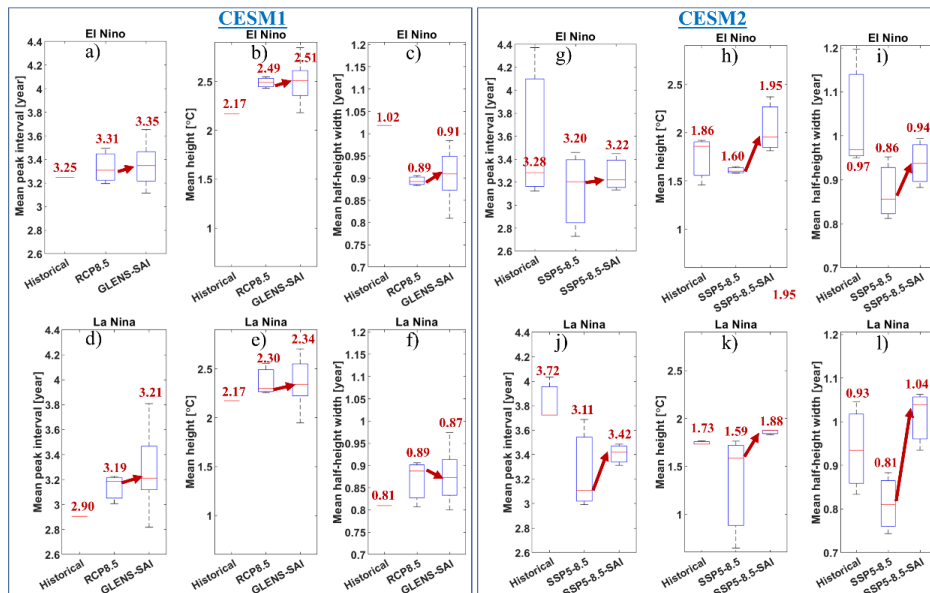
Figure 6. The projected changes in the mean peak interval, height, and half-height width of El Niño and La Niña events for global warming (RCP8.5 and SSP5-8.5) and SAI (GLENS-SAI and SSP5-8.5 -SAI) scenarios simulated by CESM1 (left panel) and CESM2 (right panel). The values

306   labeled in red on each box show their median. The red flashes are to highlight the effect that SAI has

307   on El Niño and La Niña events relative to global warming conditions.

308

309   Another way to illustrate the temporal evolution of signals is by using the power spectrum. Figures

310   7 and 8 compare the changes in temporal variability of each climate indices (AMO, NAO, ENSO, and

311   PDO) using the global power spectrums of CWTs under the global warming and SAI scenarios

312   simulated by both the CESM1 and CESM2.

313   In CESM1, the dominant mode of AMO in the historical simulation occurs in the 3-5-year band which

314   shows no significant change at the 95% level under both global warming and SAI. The historical NAO

315   has three dominant modes at 1.5 to 4 years (inter-annual), 14 years (decadal), and 21 years (inter-

316   decadal) and which also show no significant change under global warming. The dominant inter-

317   annual mode of NAO is simulated to be preserved under SAI, however, the decadal and interdecadal

318   modes present in the historical simulation and RCP8.5 disappear. For ENSO, the dominant historical

319   inter-annual modes show no significant change under both global warming and SAI. In contrast, the

320   dominant decadal mode disappears under global warming, while SAI does not effectively restore it.

321   Historical PDO also has two dominant modes, at inter-annual (i.e., 3 to 4.5 years) and near decadal (6

322   to 10 years) scales, of which the inter-annual is preserved under both global warming and SAI, but

323   the near decadal mode is weakened under global warming and SAI does not effectively restore it.
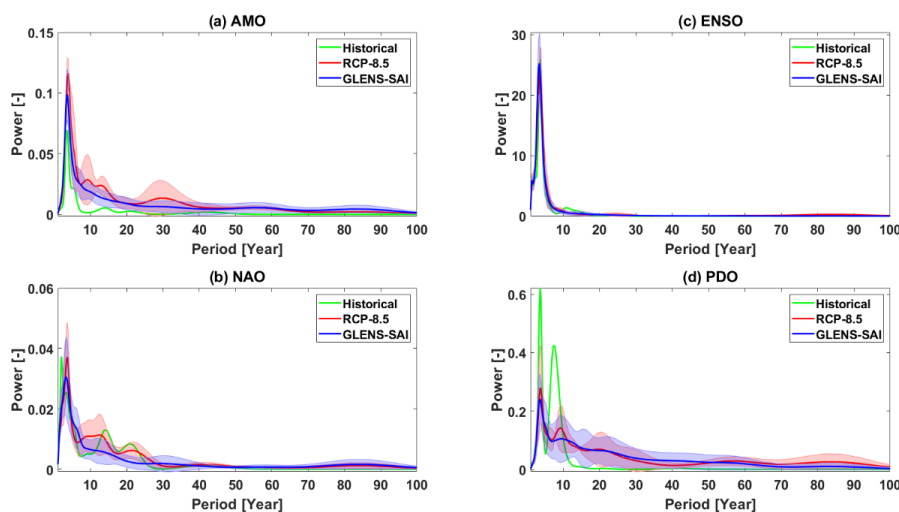
324

325   **Figure 7.** The CWT global power spectrums obtained for the indices of (a) AMO, (b) NAO, (c) ENSO,

326   and (d) PDO under RCP8.5 and GLENS-SAI compared to the historical results based on CESM1.

327   Shading in each curve shows the across-ensemble range.

328

329   In CESM1 (Fig. 7), the signals longer than 25 years, which are the most energetic modes in

330   observations of the PDO (Mantua and Hare, 2002) and AMO (Enfield et al., 2001), are not captured in

331   the historical simulations owing to their short simulation period (1980-2009). The historical period

332   simulated by CESM2 (Fig. 8) is long enough (1850-2014) to reasonably capture the low-frequency

333   signals. We therefore consider two different scenarios for the historical period based on CESM2

334   results: 1980-2009 shown in Figs. 8a-8d, upper panel (same as CESM1 (Fig. 7)) and 1850-2014

335   shown in Fig. 8, lower panel.

336   For 1980-2009 (Figs. 8a-8d, upper panel), the inter-annual modes in the historical indices, which is

337   the dominant mode in all climate indices, are preserved under both global warming and SAI, although

338   the power of the historical NAO is considerably smaller than the SSP5-8.5 and SSP5-8.5-SAI NAO (8b).

339   On the contrary, the decadal and inter-decadal signals of all the historical climate indices are not

340   preserved in the global warming scenario nor with SAI. Notably, these findings are in agreement with

341   those obtained from the CESM1 (Fig. 7).

342   In comparison with the longer 1850-2014 historical period (Figs. 8e-8h, lower panel), the inter-

343   annual modes of AMO, NAO, and ENSO are preserved under both global warming and SAI, consistent

344   with the 1980-2009 period. For the decadal and longer periodicities, SAI has a counter-productive

345   impact on AMO and NAO changes induced by greenhouse gases (Figs. 8e and 8f). For example, the

346   dominant modes at 20-30- and 55-85-year of the AMO, observed during the historical period, show

347   no significant changes under global warming; however, they vanish under SAI (Fig. 8e). Furthermore,

348   the dominant 35-55-year mode in historical NAO is roughly preserved under global warming forcing

349   (but with greater power) while it disappears under SAI (Fig. 8f). The dominant modes at 10-20- and

350   50-70-years, observed in historical PDO (consistent with the real PDO's dominant modes (Mantua et

351   al., 1997)), are not preserved under global warming and SAI does not impact them (Fig. 8h). In

352   contrast with the historical period in which the dominant modes of PDO occur in the 10-20- and 50-

353   70-year bands, the dominant modes under global warming (i.e., SSP5-8.5) and SAI (i.e., SSP5-8.5-SAI)

354   occur at the ~10-year period. The PDO shift to a higher frequency with decadal/multi-decadal

355   variability weakness, observed under global warming, was also earlier demonstrated by Fang et al.

356   (2014) with a previous generation of the climate model, the Fast Ocean Atmosphere Model (FOAM)

357   used in IPCC AR4 experiments. Likewise, the PDO timescale has been simulated to decrease from ~20

358   to ~12 years under global warming (Fedorov et al., 2020), possibly because of changes in the phase

359   speed of internal Rossby waves and ocean stratification (Zhang and Delworth, 2016). Nonetheless,

360   although PDO cycles between 30-50-year bands show slightly stronger power under SAI than global

361   warming, the 30-50-year is not the dominant PDO mode under SAI in contrast to Zhang and

362   Delworth's (2016) results for cooler climates, which the PDO dominant variability shifts to lower

363   frequency (~34 yr). They related this increase to weaker ocean stratifications accompanied by global

364   cooling. However, Zhang and Delworth (2016) used a different model (Geophysical Fluid Dynamics

365   Laboratory coupled model version 2.5 through the forecast-oriented low ocean resolution version)

366   and experiments ($2CO_2$ for global warming and $0.5CO_2$ for cooling).

367
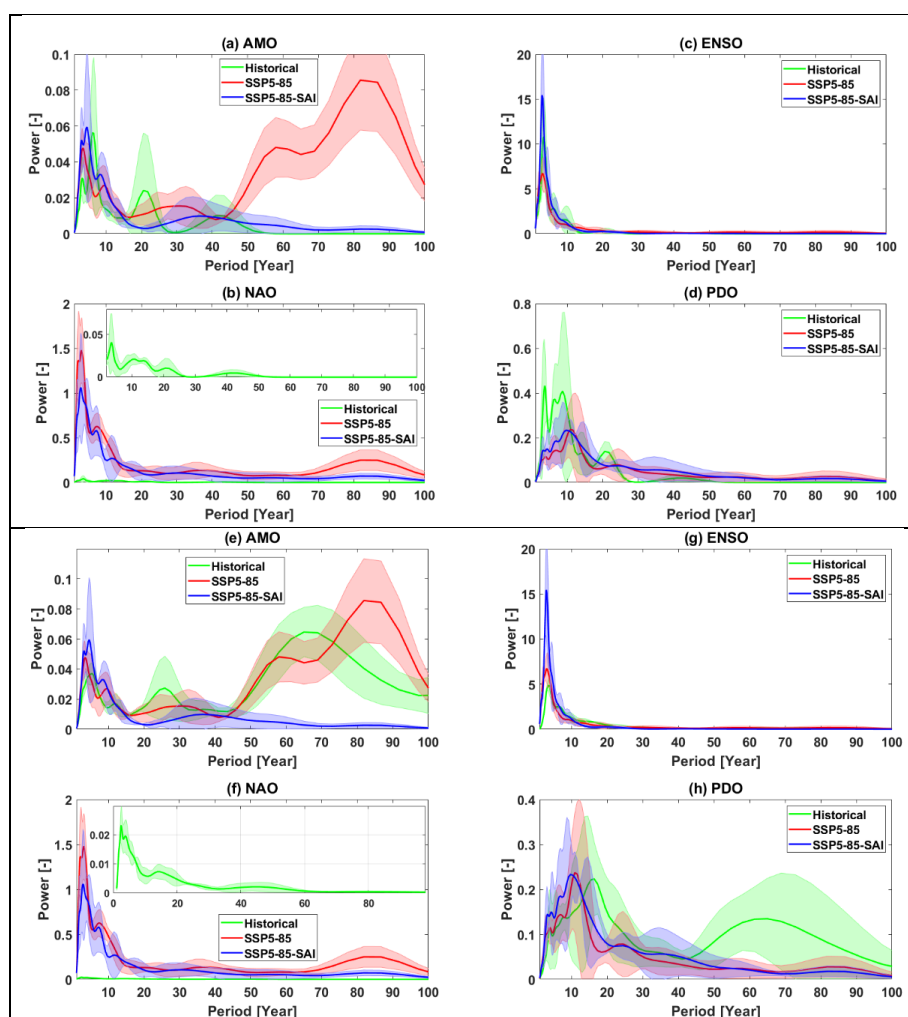
368

369   **Figure 8.** As Fig. 7 but for CESM2 under SSP5-8.5 and SSP5-8.5-SAI relative to the historical results

370   for the periods of 1980-2009 (upper panel; a to d) and 1850-2014 (lower panel; e to h). The inset

371   figure in NAO (b and f) magnifies the historical data. Shading in each curve shows the across-
372   ensemble range.

373

374   **4. Discussion**

375   **4.1. Caveats to interpretation**

376   Caution is required when interpreting the results from this study with regard to real-world

377   variability. Although CESM2 is highly rated among existing climate models, large model–observation

378   differences are nonetheless present (Fasullo, 2020). Model-observation differences are larger in the

379   earlier CESM1 version than in CESM2. For example, CESM1 exhibited a Subtropical (Azores) high

380   anomaly (related to NAO) that was too weak but its representation is improved in CESM2 (Simpson

381   et al., 2020). We also find large differences in amplitude and variance of climate indices simulated by

382   both CESM1 and CESM2 relative to the observations over the 1980-2009 period. The amplitude of

383   the dominant EOF of the ENSO-related SST-anomaly modeled in both CESM1 and CESM2 is about

384   twice the observations for the historical (1980-2009) period (Figs. S3 and S4). Figure S4 further

385   shows NAO and PDO dominant mode amplitudes are lower in the model projections than in

386   observations over the historical period. Additionally, the ENSO-associated SST anomaly pattern in

387   the tropical Pacific shows an excessive westward extension under both CESM1 and CESM2. These

388   limitations mirror those by Capotondi et al. (2020) for CESM2 in simulating the ENSO, who suggested

389   further work to illuminate how the physical parameterizations impact the key ENSO feedback.

390   Additionally, although CESM2 simulates the pattern of the summer and winter NAO well over the

391   historical period 1979-2014, the large uncertainties in specific members and in the historical

392   observations mean it is difficult to be quantitative about this (Simpson et al., 2020). However, CESM1

393   tends to underestimate the observed SST fluctuations in the Atlantic, leading to an underestimation

394   of the forced response (Undorf et al., 2018).

395   CMIP models tend to systematically underestimate the low-frequency signals (i.e., PDO) in the North

396   Pacific (Fasullo et al., 2020), owing in part to an imperfect modeling of decadal-scale structures in

397   these simulations (Masson-Delmotte et al., 2021). Compared to observational estimates, the decadal

398   variability in the subpolar North Atlantic SST appears to be slightly intensified through CMIP6

399   (Masson-Delmotte et al., 2021). How well we, therefore, can potentially capture forthcoming changes

400   in climate indices' variability will be restricted by how well each model simulates (Gabriel and

401   Robock, 2015).

402   The second limitation is disparities in the length of records (30 years for the historical period, roughly

403   90 years for greenhouse gas, and 80 years for SAI scenarios) may hinder the direct comparison of

404   climate indices behavior between historical and future climate scenarios of global warming and SAI;

405   and thus, the number of El Niño/La Niña events as well as the significance of the longer periodicities

406   (i.e., decadal and inter-decadal) in power spectrums.

407   Yet another limitation arises from the relatively low spatial resolution of the models which may affect

408   the spatial SST anomaly patterns. Furthermore, Holmes et al. (2019) pointed out the models are too

409   low resolution to resolve ocean eddies, which substantially contribute to ENSO irregularity and

410   predictability. The absence of the eddy process may also be associated with bias in spatial patterns

411   and other ENSO characteristics (Bellenger et al., 2014) in the CMIP models (Cai et al., 2021). Global

412   high-horizontal resolution climate models have been indicated to significantly improve the ocean-

413   atmosphere circulations such as ENSO (Masson et al., 2012). As an example, Haarsma et al. (2016)

414   pointed out that the High Resolution Model Intercomparison Project for CMIP6 improves the

415   understanding of the teleconnection of large-scale circulations such as ENSO, NAO, and PDO, which

416   suggests that running these high-resolution models with SAI scenario would be worthwhile.

417

418   **4.2. Implications for climate stability**

419   Teleconnection signals represent emergent properties of the non-linear climate system. The

420   behavior of the teleconnection can be characterized via its oscillations. In its simplest form, a stable

421   pattern would represent a fixed point or a periodic oscillation, but with real non-linear systems, a

422   quasi-periodic oscillation over specific frequency bands is usual (e.g., Ghil et al., 2002). These quasi-

423   periodic characteristic frequencies may change smoothly over time in a linear system but may

424   proceed towards chaotic solutions via frequency doubling (the so-called "Devil's staircase") in non-

425   linear systems. Moron et al. (1998) suggested that ENSO crossed a threshold in the early 1960s, and

426   the periodicity of the seasonally forced climatic oscillator jumped from one stage of the Devil's

427   staircase to another. The notable decline in low-frequency multi-decadal band components of the

428   wavelet spectra of the teleconnection indices we study, accompanied by a concomitant increase in

429   the variance of the decadal band is consistent with abrupt frequency doubling. This can be expected

430   in non-linear systems as the energy in the system is raised, progressing along the pathway towards

431   chaotic behavior and hence less predictability on decadal timescales. Ocean stratification (ocean

432   buoyancy frequency) and the baroclinic Rossby wave in the North Pacific play significant roles in SST

433   amplitude and PDO cycles since enhanced ocean buoyancy frequency speeds up the Rossby waves,

434   and so the decadal and longer cycle weakening accompanies higher PDO frequency (Fang et al.,

435   2014). Ocean stratification changes predominantly in response to changes in surface temperature

436   and salinity (Fang et al., 2014). The North Atlantic and the northeast Pacific are projected to be among

437   those areas with the greatest stratification changes under global warming in the second-half of the

438   21st century (Capotondi et al. 2012). Historical records also show that volcanic sulfate aerosols have

439   altered multi-decade SST variability in the North Atlantic and North Pacific (Birkel et al., 2018).

440   Whether the climate system in the model is representative of the earth can be diagnosed to some

441   extent by comparison of the historical simulation with observations. As noted in Section 4.1 both

442   CESM versions do present differences from observations, so they are clearly simulating a system that

443   is different from real climate in some ways. Previous analysis of ENSO under SAI found no significant

444   changes (Gabriel & Robock, 2015), but they used different models with widely varying fidelity of

445   modeled ENSO to actuality, and much smaller simulated quantities of SO_2 with the relatively modest

446   RCP4.5 emissions scenario as a baseline.

447   Changes in teleconnection patterns can indicate significant changes in the forcing conditions – that is

448   define what forcing is large enough to change the basic response of the system. Such changes are seen

449   in time series analysis of teleconnection indices in the real world that coincide with increased

450   greenhouse gases (Tsonis et al., 2007; Wang et al., 2009). Wang et al (2009) note that regime shifts

451   in system behavior in the observations occurred when North Pacific and North Atlantic patterns

452   increase their coupling, and the key instigator is the NAO. The NAO and its long-period counterpart,

453   the AMO, are seen in our simulations to change under SAI relative to greenhouse gas forcing at

454   periods longer than a decade.

455   The North Atlantic is an atypical region under SAI. The declines in heat transported northwards by

456   the AMOC under greenhouse gas forcing are, to great extent, reversed under all kinds of SRM

457   including SAI (Xie et al., 2022). Thus, great differences exist in SST and air/ocean heat flux between

458   SAI and greenhouse gas climates in the North Atlantic (Yue et al., 2021). If regime shifts occur when

459   North Atlantic and Pacific oceans increase their coupling, and if the decline in AMOC under

460   greenhouse gas forcing decreases coupling between the basins, then SAI may act to promote regime

461   shift by reversing a decline in AMOC.

462   Many authors have noted that explosive volcanism, in some ways a natural analogue for SAI, is

463   accompanied by a positive episode of the NAO (e.g., Robock, 2000), and this may then be associated

464   with changes in multi-decadal AMO variability (Birkel et al., 2018). Furthermore, in the extreme

465   scenario of SAI being done such that temperatures are actually decreased then the projected

466   strengthening of AMOC occurs (Tjiputra et al., 2016). However, it is also possible that regime shifts

467   induced by greenhouse gas forcing and the large temperature feedbacks they induce may dominate

468   impacts over those from fairly subtle regime shifts in teleconnection patterns. Which one may be

469   "preferable" for humanity and other species remains an open question.

5. Conclusions

This study delivers a first overview of SAI response on the large-scale ocean-atmosphere circulations of AMO, NAO, ENSO, and PDO using experiments based on CESM1(WACCM) and CESM2(WACCM6) that apply stratospheric aerosol intervention through the injection of sulfur into the stratosphere, GLENS-SAI and SSP5-8.5-SAI, respectively. The impacts of these interventions are assessed against historical (1980-2009) and projections under RCP8.5 and SSP5-85 (for the GLENS-SAI and SSP5-8.5-SAI, respectively). We found that SAI effectively reverses the global warming-imposed changes in the variance of the leading EOF SST anomaly associated with AMO, ENSO, and PDO. The SAI also effectively suppresses the changes in the spatial patterns of the EOF SST anomaly across the North Atlantic (i.e., AMO) and North Pacific (i.e., PDO). A decrease in the contrast between the cold-tongue pattern and its surroundings in the North Pacific is further projected under greenhouse gas induced global warming, which the SAI successfully restored.

CESM2 simulations suggest that increasing greenhouse gas emissions are accompanied by an increase in the frequency of the El Niño and La Niña episodes but a decrease in their intensity and duration. The SAI scenario effectively compensates for these changes.

In contrast to the impact of the SAI on the spatial patterns of the climate indices of AMO, PDO, and ENSO, the SAI scenario does not effectively suppress the projected changes in decadal and inter-decadal variability imposed by global warming. The decadal and inter-decadal variability modes of all the historical climate indices (except for Atlantic-based indices under SSP5-8.5) are not preserved in the greenhouse gas warming scenario and the SAI does not impact them.

Furthermore, compared to the historical 1850-2014 period in CESM2, SAI is projected to have a counter-productive impact on AMO and NAO at decadal and longer frequencies. Unlike the historical period in which the long-period dominant modes of PDO occur in the 10-20- and 50-70-year bands, the dominant modes under global warming are reduced to ~10-years, and the SAI does not restore them.

The results exhibited here are particular to these types of future global warming scenarios and the details of the SAI application, which deal with an extreme scenario of greenhouse gas emissions and continuous increases in sulfur emissions. Furthermore, the findings are from ensemble members from just two closely related models. Caution is due to the model-observation differences, disparities in the record length of the historical period compared to future climate scenarios, and the low spatial resolution of the models. To improve trust in the projected changes and effects of SAI on the ocean-atmosphere simulations, it is essential to further unravel the primary physical mechanisms behind

502 these changes. Nevertheless, our study does detect changes in teleconnection signals, and hence

503 underlying climate system dynamics under SAI when decomposed using EOF and wavelet analyses.

504

505 **Code/Data availability**

506 The SST and PSL data used in this study are from the CESM1 and CESM2 models and publicly available

507 from   https://www.cesm.ucar.edu/projects/community-projects/GLENS/   and   https://esgf-

508 node.llnl.gov/search/cmip6/.

509

510 **Author contributions**

511 AR, KhK, ST, and JCM conceptualized the study. AR performed the analysis and visualization. AR, KhK,

512 ST, and JCM wrote the original draft manuscript, edited the manuscript and provided feedback on the

513 interpretation of the results.

514

515 **Competing interests**

516 The authors declare that they have no conflict of interest.

517

518 **Acknowledgments**

519 We appreciate the financial support from the Solar Radiation Management Governance Initiative

520 (SRMGI; grant from DECIMALS Funds) and The World Academy of Sciences (TWAS) under grant no:

521 4500443035. We further thank Gary Strand from NCAR for his help in accessing the CESM1 model

522 outputs. Tan Mou Leong provided helpful comments and suggestions on the manuscript.

523

524 **References**:

525 Addison, P. S.: Introduction to redundancy rules: the continuous wavelet transform comes of

526   age. Philosophical Transactions of the Royal Society A: Mathematical, Physical and

527   Engineering Sciences, 376(2126), 20170258, 2018.

528 An, S. I., and Wang, B.: Inter-decadal change of the structure of the ENSO mode and its impact on the

529   ENSO frequency. Journal of Climate, 13(12), 2044-2055, 2000.

530 Bellenger, H., Guilyardi, É., Leloup, J., Lengaigne, M., and Vialard, J.: ENSO representation in climate

531   models: From CMIP3 to CMIP5. Climate Dynamics, 42(7), 1999-2018, 2014.

532 Birkel, S. D., Mayewski, P. A., Maasch, K. A., Kurbatov, A. V., and Lyon, B.: Evidence for a volcanic

533   underpinning of the Atlantic multidecadal oscillation. NPJ Climate and Atmospheric Science,

534   1(1), 1-7, 2018.

535   Cai, W., Santoso, A., Collins, M., Dewitte, B., Karamperidou, C., Kug, J. S., ... and Zhong, W.: Changing El
536   Niño–Southern Oscillation in a warming climate. Nature Reviews Earth & Environment, 2(9),
537   628-644, 2021.

538   Cai, W., Wang, G., Santoso, A., McPhaden, M. J., Wu, L., Jin, F. F., ... and Guilyardi, E.: Increased frequency
539   of extreme La Niña events under greenhouse warming. Nature Climate Change, 5(2), 132-
540   137, 2015.

541   Cai, W., Borlace, S., Lengaigne, M., Van Rensch, P., Collins, M., Vecchi, G., ... and Jin, F. F.: Increasing
542   frequency of extreme El Niño events due to greenhouse warming. Nature climate
543   change, 4(2), 111-116, 2014.

544   Capotondi, A., Deser, C., Phillips, A. S., Okumura, Y., and Larson, S. M.: ENSO and Pacific decadal
545   variability in the Community Earth System Model version 2. Journal of Advances in Modeling
546   Earth Systems, 12(12), e2019MS002022, 2020.

547   Capotondi, A., and Sardeshmukh, P. D.: Is El Niño really changing?, Geophysical Research
548   Letters, 44(16), 8548-8556, 2017.

549   Capotondi, A., Alexander, M. A., Bond, N. A., Curchitser, E. N., & Scott, J. D., Enhanced upper ocean
550   stratification with climate change in the CMIP3 models. Journal of Geophysical Research:
551   Oceans, 117(C4), 2012.

552   Chen, X., and Tung, K.K.: Global-mean surface temperature variability: Space–time perspective from
553   rotated EOFs. Climate Dynamics, 51(5), 1719-1732, 2018.

554   Cheng, L., Trenberth, K. E., Fasullo, J., Boyer, T., Abraham, J., and Zhu, J.: Improved estimates of ocean
555   heat content from 1960 to 2015. Science Advances, 3(3), e1601545, 2017.

556   Dagon, K., and Schrag, D. P.: Exploring the effects of solar radiation management on water cycling in
557   a coupled land–atmosphere model. Journal of Climate, 29(7), 2635-2650, 2016.

558   Enfield, D. B., Mestas-Nuñez, A. M., and Trimble, P. J.: The Atlantic multidecadal oscillation and its
559   relation to rainfall and river flows in the continental US. Geophysical Research
560   Letters, 28(10), 2077-2080, 2001.

561   Eyring, V., Bony, S., Meehl, G. A., Senior, C. A., Stevens, B., Stouffer, R. J., and Taylor, K. E.: Overview of
562   the Coupled Model Intercomparison Project Phase 6 (CMIP6) experimental design and
563   organization. Geoscientific Model Development, 9(5), 1937-1958, 2016.

564   Fang, C., Wu, L., and Zhang, X.: The impact of global warming on the Pacific Decadal Oscillation and
565   the possible mechanism. Advances in Atmospheric Sciences, 31(1), 118-130, 2014.

566   Fasullo, J. T., Phillips, A. S., and Deser, C.: Evaluation of leading modes of climate variability in the
567   CMIP archives. Journal of Climate, 33(13), 5527-5545, 2020.

568 Fedorov, A. V., Hu, S., Wittenberg, A. T., Levine, A. F., and Deser, C.: ENSO Low-Frequency Modulation
569   and Mean State Interactions. El Niño Southern Oscillation in a changing climate, 173-198,
570   2020.

571 Fedorov, A. V., and Philander, S. G.: A stability analysis of tropical ocean–atmosphere interactions:
572   Bridging measurements and theory for El Niño. Journal of Climate, 14(14), 3086-3101, 2001.

573 Field, C. B., & Barros, V. R. (Eds.): Climate change 2014–Impacts, adaptation and vulnerability:
574   Regional aspects. Cambridge University Press, 2014.

575 Fredriksen, H. B., Berner, J., Subramanian, A. C., and Capotondi, A.: How does El Niño–Southern
576   Oscillation change under global warming—A first look at CMIP6. Geophysical Research
577   Letters, 47(22), e2020GL090640, 2020.

578 Gabriel, C. J., and Robock, A.: Stratospheric geoengineering impacts on El Niño/Southern
579   Oscillation. Atmospheric Chemistry and Physics, 15(20), 11949-11966, 2015.

580 Ghil, M., Allen, M. R., Dettinger, M. D., Ide, K., Kondrashov, D., Mann, M. E., ... and Yiou, P.: Advanced
581   spectral methods for climatic time series. Reviews of geophysics, 40(1), 3-1, 2002.

582 Greene, C. A., Thirumalai, K., Kearney, K. A., Delgado, J. M., Schwanghart, W., Wolfenbarger, N. S., ... and
583   Blankenship, D. D.: The climate data toolbox for MATLAB. Geochemistry, Geophysics,
584   Geosystems, 20(7), 3774-3781, 2019.

585 Grinsted, A., Moore, J.C., Jevrejeva, S.: Application of the cross wavelet transform and wavelet
586   coherence to geophysical time series. Nonlinear Proc. Geoph. 11 (5-6), 561-566, 2004.

587 Haarsma, R. J., Roberts, M. J., Vidale, P. L., Senior, C. A., Bellucci, A., Bao, Q., ... and von Storch, J. S.: High
588   resolution model intercomparison project (HighResMIP v1. 0) for CMIP6. Geoscientific Model
589   Development, 9(11), 4185-4208, 2016.

590 Hamouda, M. E., Pasquero, C., and Tziperman, E.: Decoupling of the Arctic Oscillation and North
591   Atlantic Oscillation in a warmer climate. Nature Climate Change, 11(2), 137-142, 2021.

592 Holmes, R. M., McGregor, S., Santoso, A., and England, M. H.: Contribution of tropical instability waves
593   to ENSO irregularity. Climate Dynamics, 52(3), 1837-1855, 2019.

594 Hu, Z. Z., and Wu, Z.: The intensification and shift of the annual North Atlantic Oscillation in a global
595   warming scenario simulation. Tellus A: Dynamic Meteorology and Oceanography, 56(2), 112-
596   124, 2004.

597 Joyce, T. M.: One hundred plus years of wintertime climate variability in the eastern United States, J.
598   Clim., 15, 1076–1086, 2002.

599 Kravitz, B., MacMartin, D. G., Mills, M. J., Richter, J. H., Tilmes, S., Lamarque, J. F., et al.: First simulations
600   of designing stratospheric sulfate aerosol geoengineering to meet multiple simultaneous
601   climate objectives. Journal of Geophysical Research: Atmospheres, 122, 12,616–12,634, 2017.

602 Kravitz, B., Caldeira, K., Boucher, O., Robock, A., Rasch, P. J., Alterskjaer, K., ... and Yoon, J. H.: Climate
603   model response from the geoengineering model intercomparison project (GeoMIP). Journal
604   of Geophysical Research: Atmospheres, 118(15), 8320-8332, 2013.

605 Latif, M., and Keenlyside, N. S.: El Niño/Southern Oscillation response to global warming. Proceedings
606   of the National Academy of Sciences, 106(49), 20578-20583, 2009.

607 Mantua, N., and Hare, S.: The Pacific Decadal oscillation. J. Oceanogr. 58 (1), 35–44.
608   http://dx.doi.org/10.1023/A:1015820616384, 2002.

609 Mantua, N. J., Hare, S. R., Zhang, Y., Wallace, J. M., and Francis, R. C.: A Pacific interdecadal climate
610   oscillation with impacts on salmon production. Bulletin of the American Meteorological
611   Society, 78(6), 1069-1080, 1997.

612 Masson-Delmotte, V., Zhai, P., Pirani, A., Connors, S. L., Péan, C., Berger, S., ... and Zhou, B.: Climate
613   change 2021: the physical science basis. Contribution of working group I to the sixth
614   assessment report of the intergovernmental panel on climate change, 2, 2021.

615 Masson, S., Terray, P., Madec, G., Luo, J. J., Yamagata, T., and Takahashi, K.: Impact of intra-daily SST
616   variability on ENSO characteristics in a coupled model. Climate dynamics, 39(3), 681-707,
617   2012.

618 Mills, M. J., Richter, J. H., Tilmes, S., Kravitz, B., MacMartin, D. G., Glanville, A. A., et al.: Radiative and
619   chemical response to interactive stratospheric sulfate aerosols in fully coupled
620   CESM1(WACCM). Journal of Geophysical Research: Atmospheres, 122, 13,061–13,078, 2017.

621 Meinshausen, M., Lewis, J., McGlade, C., Gütschow, J., Nicholls, Z., Burdon, R., ... and Hackmann, B.:
622   Realization of Paris Agreement pledges may limit warming just below 2°
623   C. Nature, 604(7905), 304-309, 2022.

624 Moore, J. C., Yue, C., Zhao, L., Guo, X., Watanabe, S., and Ji, D.: Greenland ice sheet response to
625   stratospheric aerosol injection geoengineering. Earth's Future, ttps://doi.org/10.1029/
626   2019EF001393, 2019.

627 Moore, J. C., Rinke, A., Yu, X., Ji, D., Cui, X., Li, Y., et al.: Arctic sea ice and atmospheric circulation under
628   the GeoMIP G1 scenario. Journal of Geophysical Research: Atmospheres, 119, 567–583, 2014.

629 Moron, V., Vautard, R., and Ghil, M.: Trends, interdecadal and interannual oscillations in global sea-
630   surface temperatures. Climate Dynamics, 14(7), 545-569, 1998.

631 Riahi, K., Rao, S., Krey, V., Cho, C., Chirkov, V., Fischer, G., ... and Rafaj, P.: RCP 8.5—A scenario of
632   comparatively high greenhouse gas emissions. Climatic change, 109(1), 33-57, 2011.
633 Robock,   A.: Volcanic   eruptions   and   climate. *Reviews   of   Geophysics*, **38**(2), 191–
634   219. https://doi.org/10.1029/1998RG000054, 2000.
635 Simpkins, G.: Breaking down the NAO–AO connection. Nature Reviews Earth & Environment, 2(2),
636   88-88, 2021.
637 Simpson, I. R., Bacmeister, J., Neale, R. B., Hannay, C., Gettelman, A., Garcia, R. R., ... and Richter, J. H.:
638   An evaluation of the large-scale atmospheric circulation and its variability in CESM2 and
639   other   CMIP   models. Journal   of   Geophysical   Research: Atmospheres, 125(13),
640   e2020JD032835, 2020.
641 Shukla,   J.:   Predictability   in   the   midst   of   chaos: A   scientific   basis   for   climate
642   forecasting. science, 282(5389), 728-731, 1998.
643 Sutton, R. T., and Hodson, D. L.: Climate response to basin-scale warming and cooling of the North
644   Atlantic Ocean. Journal of Climate, 20(5), 891–907, 2007.
645 Tilmes, S., MacMartin, D. G., Lenaerts, J., Van Kampenhout, L., Muntjewerf, L., Xia, L., ... and Robock, A.:
646   Reaching 1.5 and 2.0 C global surface temperature targets using stratospheric aerosol
647   geoengineering. Earth System Dynamics, 11(3), 579-601, 2020.
648 Tilmes, S., Richter, J. H., Kravitz, B., MacMartin, D. G., Mills, M. J., Simpson, I. R., et al.: CESM1(WACCM)
649   Stratospheric Aerosol Geoengineering Large Ensemble Project. Bulletin of the American
650   Meteorological Society, 99, 2361–2371. https://doi.org/10.1175/BAMSD-17-0267.1, 2018.
651 Tjiputra, J. F., Grini, A., and Lee, H.: Impact of idealized future stratospheric aerosol injection on the
652   large-scale   ocean   and   land   carbon   cycles. Journal   of   Geophysical   Research:
653   Biogeosciences, 121(1), 2-27, 2016.
654 Trenberth, K. E.: The definition of El Niño. Bulletin of the American Meteorological Society, 78(12),
655   2771-2778, 1997.
656 Tsonis, A. A., Swanson, K., and Kravtsov, S.: A new dynamical mechanism for major climate
657   shifts. Geophysical Research Letters, 34(13), 2007.
658 Undorf, S., Bollasina, M. A., Booth, B. B. B., & Hegerl, G. C.: Contrasting the effects of the 1850–1975
659   increase in sulphate aerosols from North America and Europe on the Atlantic in the
660   CESM. Geophysical Research Letters, 45(21), 11-930, 2018.
661 Wang, G., Swanson, K. L., and Tsonis, A. A.: The pacemaker of major climate shifts. Geophysical
662   Research Letters, 36(7), 2009.

663   Wang, C., and Dong, S.: Is the basin-wide warming in the North Atlantic Ocean related to atmospheric
664   carbon dioxide and global warming?, Geophysical Research Letters, 37(8), 2010.

665   Watson, A. J., Schuster, U., Bakker, D. C., Bates, N. R., Corbière, A., González-Dávila, M., ... and
666   Wanninkhof, R.: Tracking the variable North Atlantic sink for atmospheric
667   CO2. Science, 326(5958), 1391-1393, 2009.

668   Westervelt, D. M., Conley, A. J., Fiore, A. M., Lamarque, J.-F., Shindell, D. T., Previdi, M., et al.: Connecting
669   regional aerosol emissions reductions to local and remote precipitation responses.
670   Atmospheric Chemistry and Physics Discussions, 18, 12,461–12,475.
671   https://doi.org/10.5194/acp-2018-516, 2018.

672   Xie, M., Moore, J. C., Zhao, L., Wolovick, M., and Muri, H.: Impacts of three types of solar geoengineering
673   on the Atlantic Meridional Overturning Circulation. Atmospheric Chemistry and
674   Physics, 22(7), 4581-4597, 2022.

675   Yue, C., Schmidt, L. S., Zhao, L., Wolovick, M., and Moore, J. C.: Vatnajökull mass loss under solar
676   geoengineering due to the North Atlantic meridional overturning circulation. Earth's
677   Future, 9(9), e2021EF002052, 2021.

678   Yun, K. S., Lee, J. Y., Timmermann, A., Stein, K., Stuecker, M. F., Fyfe, J. C., and Chung, E. S.: Increasing
679   ENSO–rainfall variability due to changes in future tropical temperature–rainfall
680   relationship. Communications Earth & Environment, 2(1), 1-7, 2021.

681   Zhang, L., and Delworth, T. L.: Simulated response of the Pacific decadal oscillation to climate
682   change. Journal of Climate, 29(16), 5999-6018, 2016.

683   Zhang, R., & Delworth, T. L.: Impact of Atlantic multidecadal oscillations on India/Sahel rainfall and
684   Atlantic hurricanes. Geophysical research letters, 33(17), 2006.

685

686